

Article

Functionalized Graphene-Incorporated Cupric Oxide Charge-Transport Layer for Enhanced Photoelectrochemical Performance and Hydrogen Evolution

Ambati Mounika Sai Krishna ¹, Brindha Ramasubramanian ², Sheik Haseena ³, Priyanka Bamola ⁴, Himani Sharma ⁴, Chandreswar Mahata ⁵, Alexander Chroneos ^{6,7}, Satheesh Krishnamurthy ⁸, Mahesh Kumar Ravva ³, Basavaiah Chandu ⁹, Yee-Fun Lim ^{10,11}, Avishek Kumar ¹², Seeram Ramakrishna ², Sajal Biring ^{13,14}, Sabyasachi Chakraborty ^{3,13} and Goutam Kumar Dalapati ^{2,12,13,*}

- ¹ Department of Physics, SRM University-Andhra Pradesh, Amaravati 522502, Andhra Pradesh, India
 - ² Center for Nanofibers and Nanotechnology, Mechanical Engineering Department, National University of Singapore, Singapore 117576, Singapore
 - ³ Department of Chemistry, SRM University-Andhra Pradesh, Amaravati 522502, Andhra Pradesh, India
 - ⁴ Department of Physics, School of Physical Sciences, Doon University, Dehradun 248001, Uttarakhand, India
 - ⁵ Division of Electronics and Electrical Engineering, Dongguk University, Seoul 04620, Republic of Korea
 - ⁶ Department of Electrical and Computer Engineering, University of Thessaly, 38221 Volos, Greece
 - ⁷ Department of Materials, Imperial College London, London SW7 2AZ, UK
 - ⁸ School of Engineering and Innovation, The Open University, Milton Keynes MK7 6AA, UK
 - ⁹ Department of Nanotechnology, Acharya Nagarjuna University, Guntur 522510, Andhra Pradesh, India
 - ¹⁰ Institute of Materials Research and Engineering, Agency for Science, Technology and Research (A*STAR), 2 Fusionopolis Way, Innovis, Singapore 138634, Singapore
 - ¹¹ Institute of Sustainability for Chemical, Engineering and Environment, Agency of Science, Technology and Research (A*STAR), 1 Pesek Road, Singapore 627833, Singapore
 - ¹² Sunconnect, 1 Cleantech Loop, Singapore 637141, Singapore
 - ¹³ Organic Electronics Research Center, Ming-Chi University of Technology, 84 Gungjuan Rd., New Taipei City 24301, Taiwan
 - ¹⁴ Department of Electronic Engineering, Ming-Chi University of Technology, 84 Gungjuan Rd., New Taipei City 24301, Taiwan
- * Correspondence: gkd@nus.edu.sg



Citation: Krishna, A.M.S.; Ramasubramanian, B.; Haseena, S.; Bamola, P.; Sharma, H.; Mahata, C.; Chroneos, A.; Krishnamurthy, S.; Ravva, M.K.; Chandu, B.; et al. Functionalized Graphene-Incorporated Cupric Oxide Charge-Transport Layer for Enhanced Photoelectrochemical Performance and Hydrogen Evolution. *Catalysts* **2023**, *13*, 785. <https://doi.org/10.3390/catal13040785>

Academic Editors: Sekar Karthikeyan, Boopathy Ramasamy and Bishweshwar Pant

Received: 27 February 2023

Revised: 7 April 2023

Accepted: 19 April 2023

Published: 21 April 2023



Copyright: © 2023 by the authors. Licensee MDPI, Basel, Switzerland. This article is an open access article distributed under the terms and conditions of the Creative Commons Attribution (CC BY) license (<https://creativecommons.org/licenses/by/4.0/>).

Abstract: The production of hydrogen (H₂) through photoelectrochemical water splitting (PEC-WS) using renewable energy sources, particularly solar light, has been considered a promising solution for global energy and environmental challenges. In the field of hydrogen-scarce regions, metal oxide semiconductors have been extensively researched as photocathodes. For UV-visible light-driven PEC-WS, cupric oxide (CuO) has emerged as a suitable photocathode. However, the stability of the photocathode (CuO) against photo-corrosion is crucial in developing CuO-based PEC cells. This study reports a stable and effective CuO and graphene-incorporated (Gra-COOH) CuO nanocomposite photocathode through a sol-gel solution-based technique via spin coating. Incorporating graphene into the CuO nanocomposite photocathode resulted in higher stability and an increase in photocurrent compared to bare CuO photocathode electrodes. Compared to cuprous oxide (Cu₂O), the CuO photocathode was more identical and thermally stable during PEC-WS due to its high oxidation number. Additionally, the CuO:Gra-COOH nanocomposite photocathode exhibited a H₂ evolution of approximately 9.3 μmol, indicating its potential as a stable and effective photocathode for PEC-WS. The enhanced electrical properties of the CuO:Gra-COOH nanocomposite exemplify its potential for use as a charge-transport layer.

Keywords: cupric oxide (CuO); graphene; photocathode; photoelectrochemical (PEC); hydrogen (H₂); charge-transfer layer; stability

1. Introduction

Enhanced and sustainable solar energy production is essential to support increasing consumption and environmental requirements [1–6]. In that respect, efficient catalysts play an important role in their overall performance. The most functional catalysts for green hydrogen (H_2) production via water splitting (WS) (thermodynamic potential of 1.23 V) are generally metallic or semiconductor materials [7]. A low-cost semiconducting photocatalyst with outstanding aqueous-electrolyte stability and high visible-light absorption is always envisioned as the best material for such applications [8]. In photoelectrochemical water splitting (PEC-WS), the light energy is absorbed by a semiconductor material to form electron–hole pairs, and the photo-induced electrons (or holes) are directed to the semiconductor/solution interface by the space-charge field, where they reduce (or oxidize) water [9–13]. On the other hand, a photocathode should be a p-type semiconductor for the hydrogen evolution reaction (HER), which means the conduction band edge is more inclined towards the negative than the potential of H_2O/H_2 [9–14]. Among other semiconducting materials, cupric oxide (CuO) [15–17] can be an ideal candidate for such applications as it is a p-type semiconductor that is abundant, inexpensive and has appropriate optical and electronic properties for photovoltaic (PV) [18] or photoelectrochemical (PEC) [19] applications. In particular, CuO thin films demonstrated 2–3 times enhanced PEC performance along with increased transmittance and electrical conductivity [20]. The advantages of CuO as a material for solar-cell applications include a suitable band gap (1.3–1.5 eV), [21] high optical absorption, a maximum theoretical efficiency of 31%, low cost and terawatt-level scalability [22]. Additionally, hydrogen produced via solar energy is an important, relatively clean fuel that can be used in fuel cells. The research community focuses on creating high-efficiency visible-light photocatalysts that can harness solar light effectively [23–28] and can be integrated with photovoltaic devices for green hydrogen production.

Cupric oxide (CuO) has shown higher photoconversion efficiency than other copper oxide phases, but it readily changes to cuprous oxide (Cu_2O), an unstable photocathode [29]. In addition, these Cu_2O molecules possessed a high electron–hole recombination rate, which hindered them from being very efficient in the hydrogen evolution reaction [20]. As a result, research focusing on CuO-based photocathodes must be developed in order to reduce or prevent the occurrence of the Cu_2O phase during WS and increase photo-corrosion stability. Furthermore, apart from the stability issue, synthesizing the photocathode for a large area is another challenge [30,31]. To tackle these difficulties, a low-cost, high-yield electrode production technology is required. Therefore, CuO was synthesized via sputtering and a solution-based thin-film deposition technique to address these issues [15,32–34]. In general, a thin film deposited via sol-gel has a slow charge-transfer rate, high bulk resistance and a high photogenerated-carrier recombination rate [35]. However, we aimed to incorporate graphene into metal oxide thin films for better improvement in the charge-transfer efficiency [36–38].

Importantly, CuO exhibits an ideal band alignment, with a minimum conduction band of approximately -0.8 V to -1.0 V vs. the reversible hydrogen electrode (RHE) for water reduction reactions. CuO's photocatalytic performance is limited by the charge carrier's rapid recombination rate and the lack of production of reactive oxygen species. Chemical modification of CuO can be used to prevent charge recombination, which can boost photocatalytic efficiency. The incorporation of graphene-based materials with CuO is one such strategy that addresses these difficulties. Generally, graphene oxide (GO) is one of the most significant graphene derivatives due to its properties, such as strong mechanical strength, suitable redox reaction, stability, a large surface area and excellent conductivity [39,40]. It also contains abundant epoxides (C–O–C), C–OH and terminated COOH groups [41]. Graphene is also known to be used in nanocatalysis, which supports the synthesis of effective heterogeneous catalysts [42,43]. Its exceptional conductivity can ease electron transfer during transformations [44]. The structure of graphene is hexagonal (sp^2 -hybridization), also having excellent mechanical properties and high thermal conductivity

and giving rise to ultrahigh electrical conductivity, which is an attractive point in the research field for various energy-conversion applications. Heteroatom-doped graphene has a high electrocatalytic activity, which is a remarkable characteristic with great promise for hydrogen generation via photocatalytic materials [45]. Its electron charge carriers exhibit an enormous intrinsic mobility and an undersized effective mass (which is zero) and can also travel up to a micrometer (μm) distance without scattering at RT (room temperature). When compared to copper, graphene has six times higher current densities and record stiffness and thermal conductivity [46].

As an electron acceptor or transporter, graphene can assist in separating the photogenerated electron-hole pairs in semiconductors as well as efficiently transport photogenerated electrons to reactive sites, potentially improving photocatalytic H_2 production. With the use of surface functional groups (epoxides, hydroxyls, carbonyls, etc.) and lattice defects (vacancies, holes) in chemically transformed structures, graphene can anchor and immobilize metal nanoparticles on its surface for further applications [47,48]. Combining semiconductors with graphene reduces the problem of photo-corrosion because graphene's electron acceptor/transport roles are advantageous for swiftly removing light-induced charges from semiconductors. The catalytic activity of graphene-supported catalysts will be enriched as the charge transfer augments from graphene to the catalysts [49]. A recent study [50] indicates that incorporating graphene on top of CuO will dramatically enhance its photostability as well as photocatalytic activity. By means of functionalization or charge transfer between graphene and CuO nanostructures, one can introduce a new feature into the formation of CuO nanostructures that possess the enhancement of H_2 evolution. Since it remains challenging to investigate the interactions between graphene and CuO at the molecular scale using experimental techniques, the insight brought by density functional theory (DFT) studies can provide a better understanding of charge transfer between graphene and CuO [51–54].

Thus, in the present study, a combination of experimental and computational studies has been carried out to gain a better understanding of CuO functionalized graphene nanostructures. Initially, CuO thin film is incorporated with graphene nanosheets (a sol-gel precursor solution with functionalized graphene nanostructures) via spin coating. Especially, we have incorporated -COOH functionalized graphene onto the CuO to enhance its efficiency and stability as a photocathode. The primary objective of this research is to use sol-gel spin coating to achieve high film performance and good crystal quality. Furthermore, improved electrical and optical properties, along with increased charge transport of CuO (CuO:Gra-COOH) thin film on FTO, are reported, with increased overall H_2 evolution efficiency. DFT calculations have also been performed on CuO and functionalized graphene complexes to gain insights into their electronic properties.

2. Results and Discussion

2.1. Structure Elucidation of Active Thin Film

The microstructural properties of sol-gel-deposited CuO thin film (~20 nm) and CuO:Gra-COOH thin film were evaluated by Transition Electron Microscopy (TEM). The TEM images of the CuO thin film and the CuO:Gra-COOH thin film that were deposited on the FTO substrate are shown in Figure 1. Figure 1a shows the sol-gel-deposited CuO on sputter-grown CuO (500 nm) and Figure 1b shows the sol-gel-deposited CuO:Gra-COOH on sputter-grown CuO (500 nm). As a result, Figure 1b shows that the composite of CuO and Gra-COOH was successfully incorporated and that it was developed on a sputter-grown CuO (500 nm) substrate. It was also observed that graphene nanoparticles are sorted out as spherical particles with a diameter of approximately 5 nm. Furthermore, the polycrystallinity of the CuO particles was confirmed by the HRTEM image in Figure 1c. The Fast Fourier transform (FFT) shows the crystalline structure of the film, and the FFT of the CuO:G-COOH thin film specifies the spatial frequency distribution. In particular, the central point indicates the brightness of the picture (because the central area is proportional to the low frequency), as can be seen in Figure 1c,e. Thus, as shown in Figure 1c,e, each

power spectrum resembles an orientation, implying that pore structures are randomly oriented. To examine the pore structure in greater depth, a masking step and FFT were applied to the power spectra. A ring-shaped mask pattern specifies a peculiar frequency region in reciprocal space, and then an FFT is performed, resulting in images with different pore-size ranges. Two FFT areas are present in the CuO:Gra-COOH diameter of 5 nm. The distinctive plane (111) of CuO is seen in the SAED patterns (Figure 1c). The individual particle's HRTEM image shows a lattice spacing of 0.234 nm (FFT area (1)), which is consistent with the (111) plane of monoclinic CuO. Similarly, as shown in Figure 1e, the pore size of FFT area (2) is 0.273 nm for the (002) plane (inner) of graphene, 0.229 nm for the (111) plane (middle) and 0.201 nm for the (002) plane (outer) of monoclinic CuO. However, we have carefully excluded these structures from further evaluation as they did not show additional potential results in our theoretical calculations, which are presented in the next section. The composite nature of CuO has been confirmed by TEM and HRTEM analyses. The existence of nano-sized CuO in Gra-COOH indicates that its energetics are favorable for water reduction (i.e., H₂ generation).

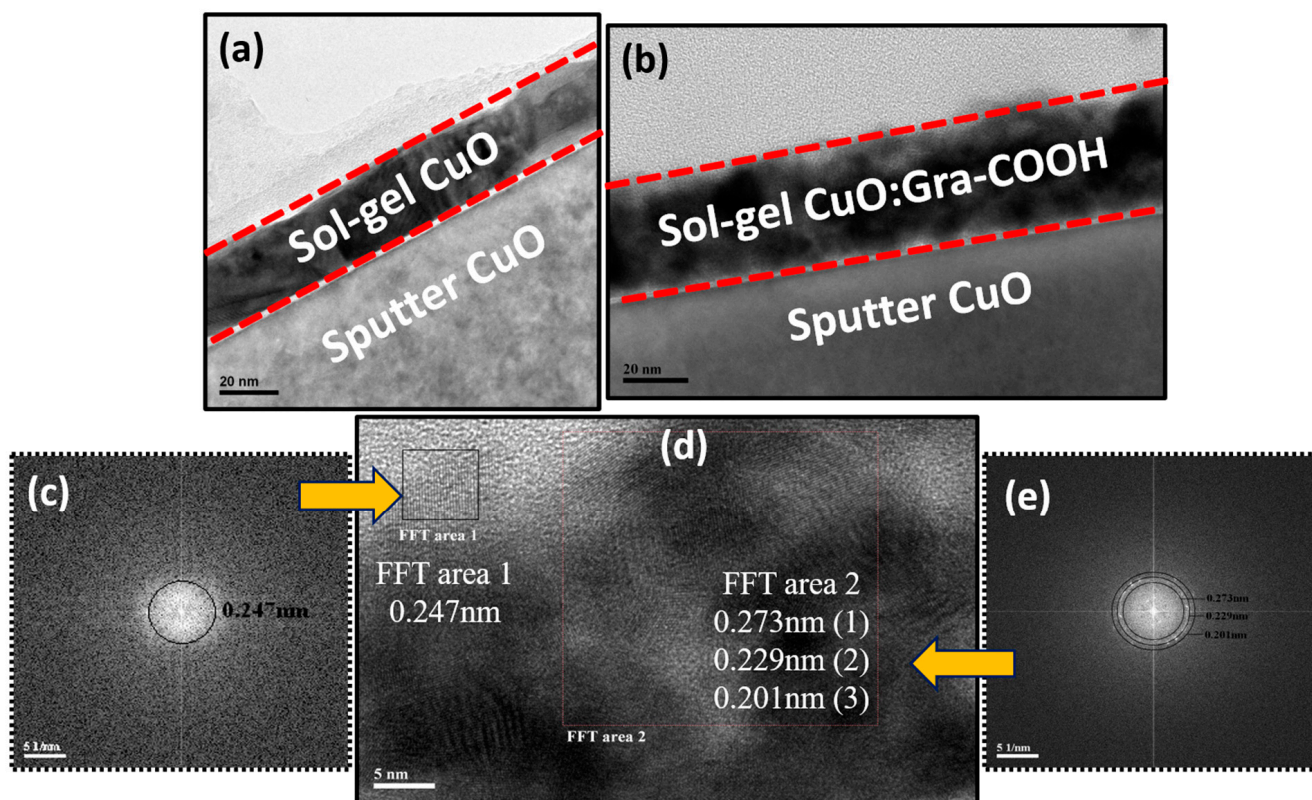


Figure 1. Cross-sectional and TEM images: (a) sol-gel-deposited CuO (~20 nm); (b) sputter-grown sol-gel spin-coated CuO:Gra-COOH thin film; and (c–e) FFT calculations of CuO:Gra-COOH thin film.

The structural detail of sputter-grown sol-gel-deposited CuO and CuO:Gra-COOH was analyzed using X-ray diffraction (XRD) analysis, and the spectra are shown in Figure 2. The crystalline size (D) of the samples was calculated using the Debye–Scherrer formula.

$$D = \frac{0.94 \lambda}{\beta \cos \theta}$$

where, λ is the wavelength of the XRD radiation;

β is the full width at half maximum (FWHM) of the peak, which corresponds to a plane;

θ is the angle obtained from the 2θ value, which corresponds to the XRD pattern.

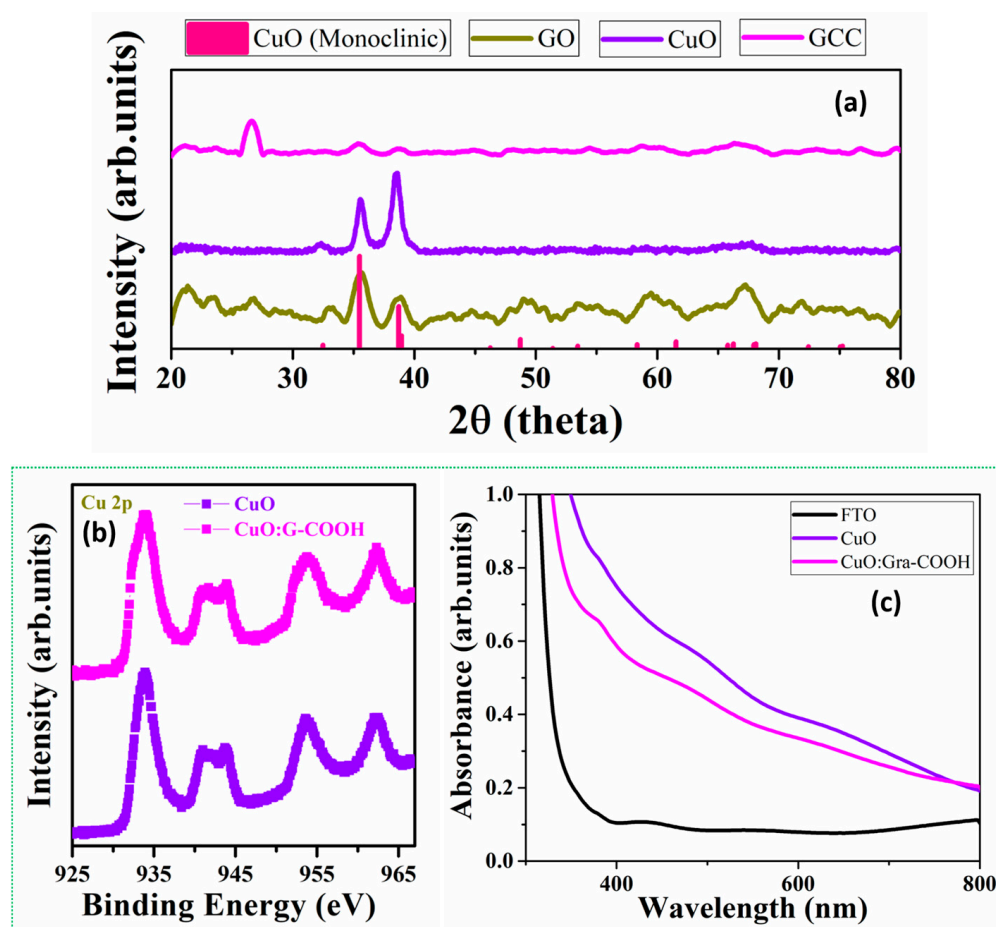


Figure 2. (a) XRD spectra of sputter-grown CuO (500 nm) on FTO and sputter-grown sol-gel spin-coated CuO:Gra-COOH (20 nm) on FTO photoelectrodes, which are matched with monoclinic CuO; (b) XPS spectra of CuO and CuO:G-COOH; and (c) UV-visible spectra of FTO, CuO and CuO:G-COOH. CuO—Copper Oxide, GCC—Gra-COOH/CuO.

According to the XRD spectra, the highest intensity peaks of the sol-gel-deposited CuO and CuO:Gra-COOH films at 2θ values are 38.5 and 35.6, which are attributed to the (111) and (002) planes, respectively. These results are consistent with the CuO monoclinic structure (JCPDS# 05-0661). As a result, it appears that the dominant phase is CuO, and graphene oxide did not form in the film. In the case of GCC (Gra-COOH/CuO), the highest intensity peak was observed at 26.64 (2θ value), which is the graphene peak [55,56]. For CuO, peaks at 2θ values of 38.5 (111) and 35.6 (002) were observed. CuO:G composites have a distinct diffraction peak along with pure CuO characteristic peaks, implying that the CuO in the CuO:G composites has good crystallinity. Additionally, oxygen functional groups such as the carboxylic (–COOH) group present on the surface of graphene prevent CuO grain diffusion and further crystallization to Cu₂O [57]. As seen in Figure 2a, the graphene peak was more prominent than CuO due to the thickness of the –COOH-functionalized graphene (20 nm) and CuO (500 nm). Furthermore, by integrating functionalized graphene (–COOH) with CuO, phase transformation during PEC can be significantly diminished, leading to enhanced photo-corrosion stability of the CuO photocathode, which results in an enhancement in the evolution rate of H₂. Hence, the crystallinity of sol-gel-deposited CuO and CuO:Gra-COOH thin films was studied by XRD. Next, to know about the morphology of the film, we performed AFM, which is detailed in the next section.

Figure 2b shows the XPS spectra of CuO and CuO:G-COOH thin films. Satellite peaks are seen at energies between 943 and 951 eV and between 957 and 969 eV. Additionally, all films show prominent Cu2p_{3/2} and Cu2p_{1/2} peaks at 932.7 and 954.5 eV, respectively,

confirming the establishment of the CuO-dominating phase. Tiny shoulder peaks at 933.3 eV and 954.1 eV are visible for CuO and CuO:G-COOH films, which have values much lower than those of bare CuO. Before evaluating how well CuO and CuO:G-COOH split water, this study looks at how well they can absorb visible light. Due to the low bandgap of CuO, both the CuO and CuO:G-COOH electrodes exhibit outstanding light-absorption capabilities. The visible-light absorption starts at approximately 800 nm (as seen in Figure 2c), with increased absorption capabilities at shorter wavelengths. The CuO film's functionalized graphene causes the light absorption spectra's peak to shift considerably (by approximately -50 nm) to shorter wavelengths. Thus, we expect functionalized films to have better light-harvesting abilities.

In general, photocatalytic activity is influenced by the morphology of materials to a great extent. In order to understand the surface morphology, crystal structure, grain size and roughness of the CuO:Gra-COOH photoelectrode, atomic force microscopy (AFM) studies were carried out, as shown in Figure 3. Figure 3a shows the 2D AFM image, and Figure 3b shows the 3D view of spherical particles with aggregations at different magnification ranges of 10–100 nm. It is observed that the nanoparticles are scattered without any clustering and that the surface morphology of the film is highly homogenous. Figure 3c depicts a clear image of a cross-section at high resolution, and Figure 3d corresponds to the appropriate cross-section profiles indicated by lines. Basically, grain size was influenced by the interaction between nucleation and growth rates. The topographic map reveals that the nanoparticles' surfaces are spherical in shape. The rough surfaces have a higher number of active sites and a relatively larger surface area. Compared to recombination, a rough-surface film is expected to have a larger electrode or electrolyte interfacial area, which increases charge-transport rates. As a result, because it inhibits the recombination of photogenerated charge carriers, this type of film can play a vital role in PEC activity.

In order to gain insights into the electronic properties of functionalized graphene and CuO complexes, DFT calculations were carried out on the CuO clusters and a representative graphene monolayer. The DFT results focused on how the chemical functionalization of graphene impacts the CuO and graphene-layer interactions. Thus, geometric optimization of the pristine graphene model and its carboxyl and amine derivatives was carried out using the B3LYP-D/6-31G** level of theory, as depicted in Figure 4.

It can be seen from the optimized geometries that the CuO cluster shape is rearranged after adsorption on the graphene layer. Table 1 shows the calculated energy levels of the highest occupied molecular orbital (HOMO) and lowest unoccupied molecular orbital (LUMO), as well as the HOMO–LUMO gap (Eg), for various CuO-Graphene complexes. As one can expect, the functionalization of graphene with carboxylic and amine groups alters the HOMO and LUMO energy values. The electron-donating amine group destabilizes the HOMO level (from -4.92 eV to -4.64 eV), and the electron-withdrawing carboxylic acid group stabilizes the HOMO level (from -4.92 eV to -5.16 eV). Figure 5 depicts the pictorial representations of single-electron HOMO and LUMO wavefunction distributions. In the case of CuO@Gra-COOH, we observed a strong wavefunction delocalization between CuO and the graphene layer. The strong wavefunction overlap between CuO and graphene-COOH could be the reason for the stable CuO@Gra-COOH complex. Figure 6 shows the density of states (DOS) for various CuO-Graphene complexes. Graphene-incorporated CuO (CuO@Gra-COOH) film showed better performance compared to CuO@Gra. The stronger overlap of CuO cluster orbitals with the graphene layer is evident from the DOS calculations.

Additionally, the charge distribution for CuO-Graphene complexes was calculated using Mulliken population analysis. Mulliken charges were calculated based on the charge population that each atom defines as its basic functions [58]. Figure 7 shows the Mulliken charge distribution for various CuO-Graphene complexes produced by the B3LYP-D/6-31G** level of theory. We observed charge transfer from graphene to CuO clusters. The calculated charge distribution for the CuO-Gra and CuO-Gra-NH₂ complexes showed an almost similar

charge distribution ($-0.83 |e|$), whereas in the case of CuO@Gra-COOH, the calculated charge distribution was $-0.81 |e|$.

Table 1. Calculated energy levels of HOMO and LUMO and energy difference (ΔE) for various CuO-Graphene complexes.

S. No.	Sample Name	E_{HOMO}	E_{LUMO}	ΔE
1	CuO@Gra	-4.92 eV	-4.19 eV	0.73
2	CuO@Gra-COOH	-5.16 eV	-4.38 eV	0.78
3	CuO@Gra-NH ₂	-4.64 eV	-3.92 eV	0.72

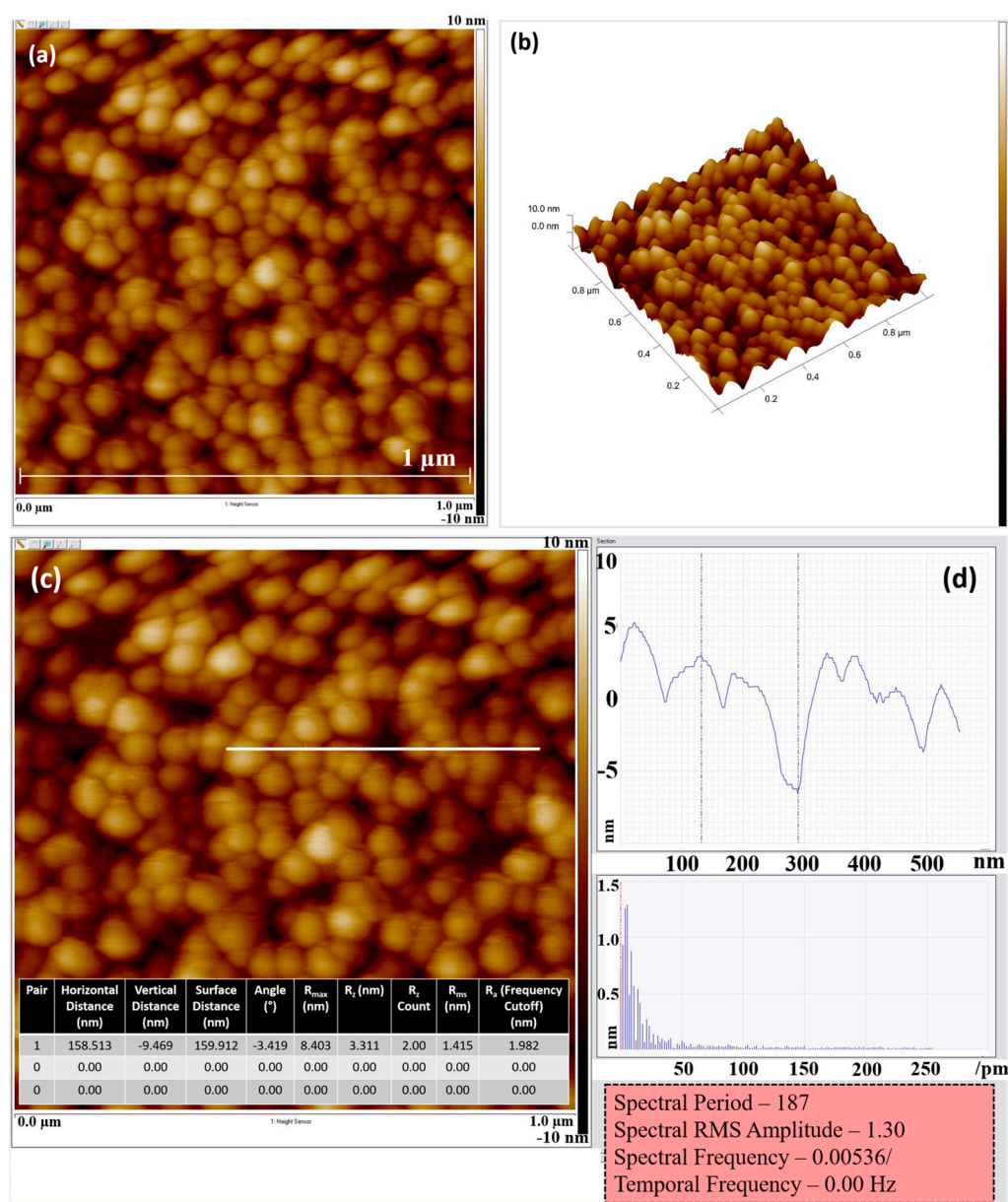


Figure 3. AFM images of CuO:Gra-COOH photoelectrode: (a) CuO:Gra-COOH in two dimensions; (b) CuO:Gra-COOH in three dimensions; (c) CuO:Gra-COOH cross-section at high resolution; (d) cross-section profiles in the AFM images that correspond to the appropriate cross-section profiles indicated by lines.

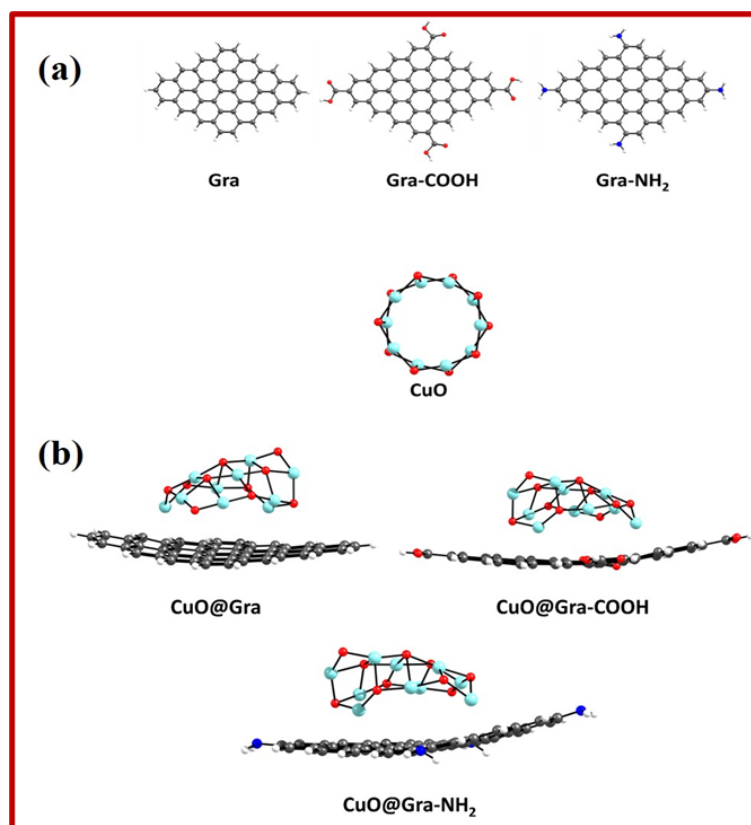


Figure 4. (a) Optimized geometries of pristine graphene sheet (Gra), carboxylic acid functionalized graphene (Gra-COOH), amine functionalized graphene (Gra-NH₂) and CuO cluster; (b) optimized geometries of CuO@Gra, CuO@Gra-COOH and CuO@Gra-NH₂ complexes. Grey, Cyan, Red, Blue and White color represents C, Cu, O, N, and H atoms.

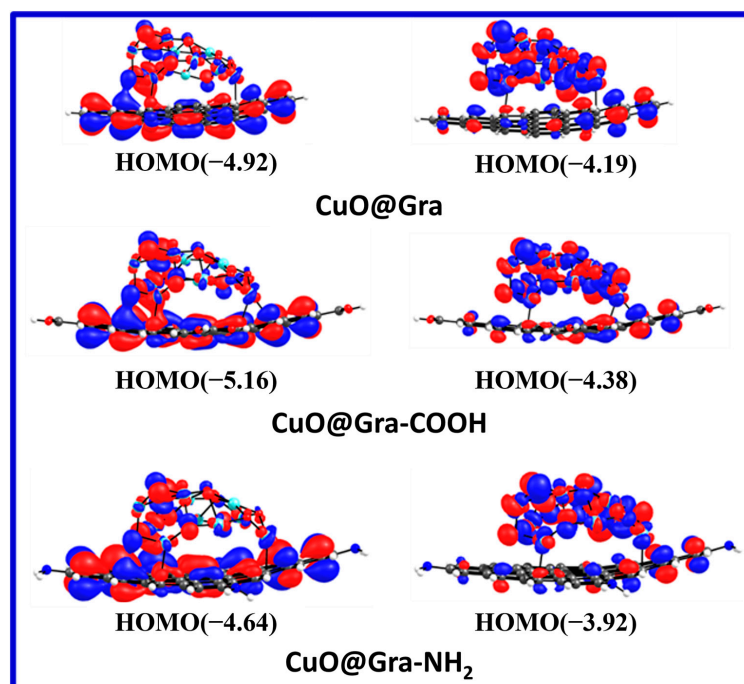


Figure 5. Pictorial representations of a single-electron HOMO and the LUMO wavefunction distributions for various CuO-Graphene complexes. Grey, Cyan, Red, Blue and White color represents C, Cu, O, N, and H atoms.

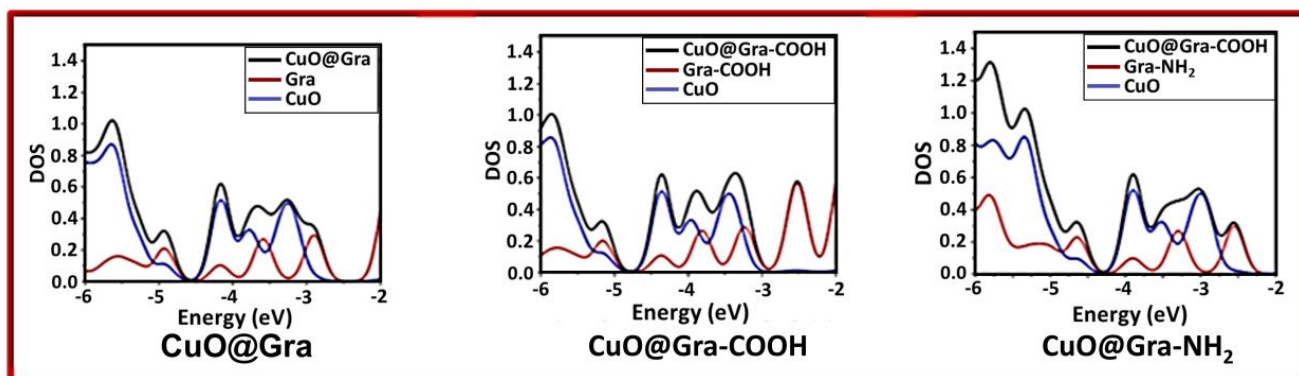


Figure 6. Density of states for various CuO-Graphene complexes.

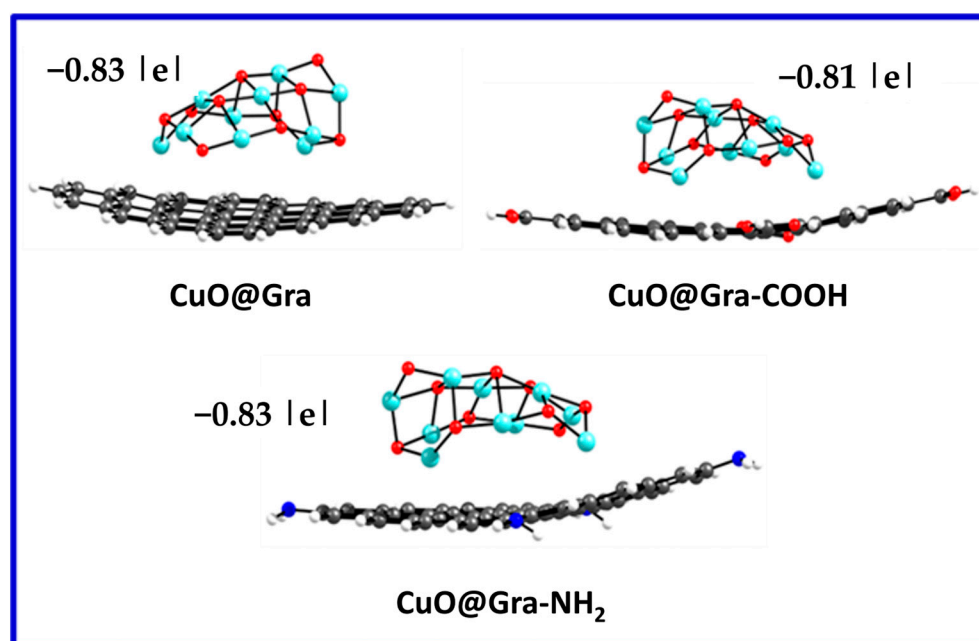


Figure 7. Mulliken charge distribution for various CuO-Graphene complexes. Grey, Cyan, Red, Blue and White color represents C, Cu, O, N, and H atoms.

2.2. PEC Property Comparison of CuO and Incorporated Graphene CuO Thin Film

The effect of CuO and CuO:Gra-COOH thin-film crystallinity on the performance of PEC-WS was investigated. The I-V characteristics (current vs. voltage) of the PECs were measured in two conditions (on and off): “light on” under AM 1.5G illumination of 100 mW/cm² and “light off” in darkness. The measured potential was converted into a reversible hydrogen electrode (RHE) scale by using the following equation:

$$E(\text{RHE}) = E(\text{Ag}/\text{AgCl}) + 0.197 + 0.059 \text{ pH}$$

$E(\text{Ag}/\text{AgCl})$ and $E(\text{RHE})$ are measured potentials with respect to the Ag/AgCl R.E and RHE scales, respectively. In our experiment, a pH of 5.84 was maintained, corresponding to the pH of the electrolyte. Due to the presence of dissolved oxygen (O₂), which would result in oxygen reduction rather than H₂ creation as a primary cathodic reaction, the system was bubbled with argon (Ar) gas for 1 h prior to the PEC measurements. Figure 8 shows Current-Voltage (I-V) characteristics of a 500 nm sputter CuO photocathode with a CuO and CuO:Gra-COOH charge-transfer layer under light-on and -off conditions. After incorporating Gra-COOH, linear cyclic voltammetry showed an improvement in photocurrent. Under chopped visible-light conditions, I-V plots were recorded at a fixed

potentiality, and the photocurrent was recorded at -2.6 mA/cm^2 at 0 V vs. RHE. The photocurrent of the electrode was determined by the rate of recombination at the electrolyte or electrode interface and efficiency. The excited electrons were transferred from the semiconductor to the FTO substrate [59].

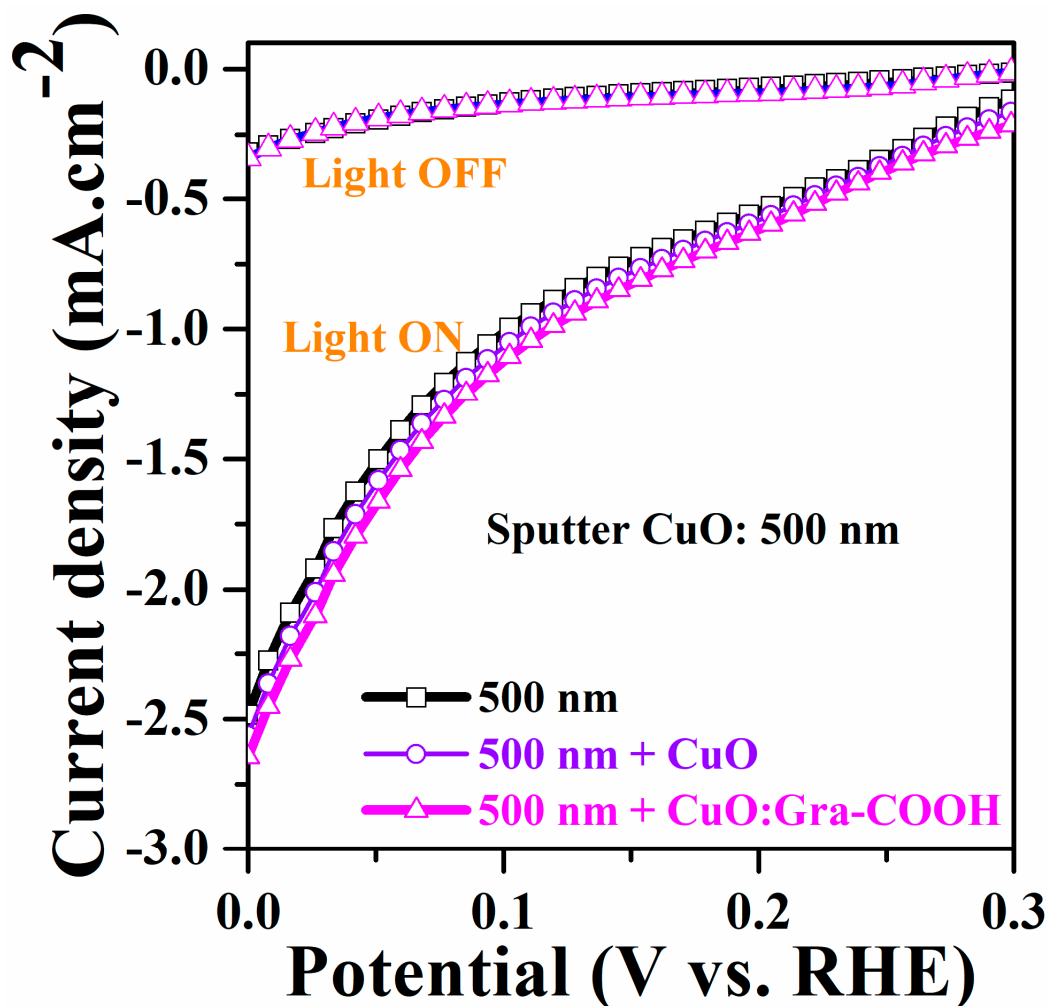


Figure 8. Current-Voltage characteristics of a 500 nm sputter CuO photocathode with sol-gel spin-coated CuO and CuO:Gra-COOH charge-transfer layer.

A functionalized Gra-COOH-incorporated CuO electrode shows a slightly higher dark current compared to sputter CuO. However, it does not show an enormous reduction in photocurrent after numerous cycles of light-on and -off conditions. As previously stated, the -COOH functional group acts as an electron acceptor group [60] and has strong electron-accepting capabilities, [61,62] which can enhance the p-type conductivity of the hybrid structure. It has also been demonstrated that the efficiency of charge separation improves when graphene is present [63–65]. Under illumination, CuO is known to be unstable and will eventually reduce into Cu_2O , while Cu will decrease the photocurrent over time. The incorporated graphene CuO working electrode (CuO:Gra-COOH) contributes to a stable photocurrent in spite of having a similar light-harvesting profile [31].

One of the major concerns with CuO-based working electrodes for PEC-WS applications is their instability in aqueous electrolytes. Figure 9 shows the photo-corrosion stability of a 500 nm sputter CuO photocathode with a CuO and CuO:Gra-COOH charge-transfer layer under light-on and -off conditions. As seen in Figure 9, CuO shows a $\sim 20\%$ decrease in photocurrent after 900 s, while the CuO:Gra-COOH electrode only shows a $\sim 10\%$ reduction. Particularly, the stability of the photocathode also depends on the quantum of Gra-COOH,

which generates only 10–20% of the initial photocurrent. Although it is a ~10% reduction in photocurrent, the CuO:Gra-COOH electrode performs better, which should be noticeable. If a film has a good crystalline layer, it exhibits enhanced photostability due to the superior transit of photogenerated electrons (e^-) and holes (h^+) to the surface. This allows the photogenerated charges to move more rapidly from the electrode to the electrolyte. After adding CuO:Gra-COOH, the photogenerated carriers exhibit a tendency to transport rapidly from the electrode's bulk to the electrolyte. This can be attributed to the improved electrical conductivity of CuO through the addition of graphene (CuO:Gra-COOH). As a result, nanocrystal-engineered CuO thin films can improve the efficiency of CuO-based PEC-WS as well as the stability of the photocathode.

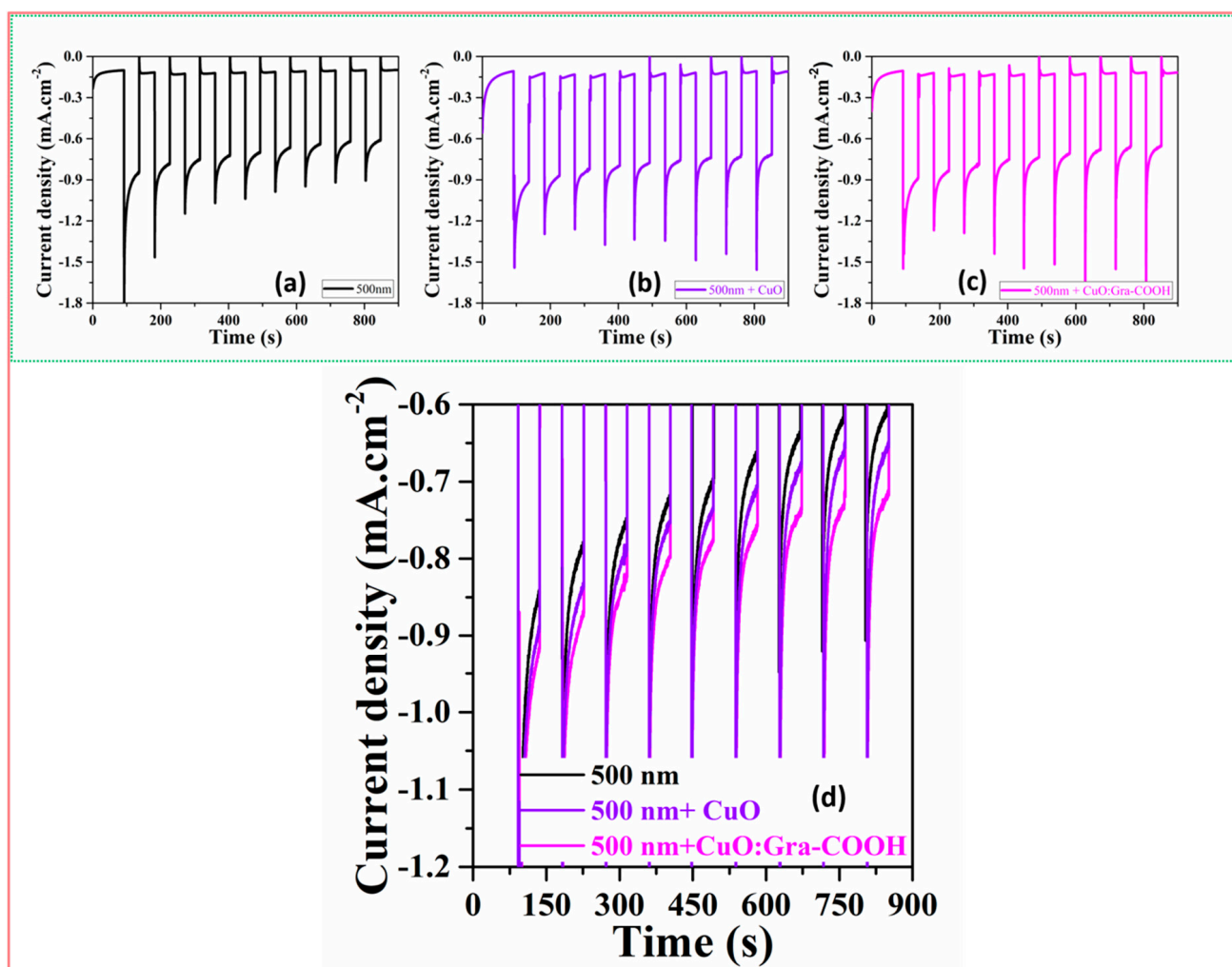


Figure 9. (a) Photo-corrosion stability test of 500 nm sputter-coated CuO photocathode (black); (b) 500 nm sputter-coated CuO photocathode with spin-coated CuO (20 nm) (blue); (c) 500 nm sputter-coated CuO photocathode with sol-gel spin-coated CuO:Gra-COOH (20 nm) (magenta); (d) photo-corrosion stability test of all CuO thin films.

In consequence, an optimized CuO:G-COOH photocathode would be ideal for solar H₂ generation because it would conflate charge-transport properties and photogenerated carriers of CuO [24]. Figure 10 shows the hydrogen evolution under light illumination of a 500 nm sputter CuO and a 500 nm sputter CuO with sol-gel-deposited Cu and a CuO:Gra-COOH charge-transfer layer. As can be seen in the figure, there is no difference between sputter-grown CuO (500 nm) and sputter-grown CuO (500 nm)/sol-gel CuO (20 nm). However, in the case of CuO:Gra-COOH, the ratio is 10% higher, and the amount of hydrogen

evolution is $\sim 9.3 \mu\text{mol}$. The calculated faradic efficiencies of CuO and CuO:Gra-COOH for the PES process, as shown in Figure 10, are 79% and 84%, respectively, using the equations from [66]. A low-cost, highly stable photocathode is required for the generation of solar-driven H_2 . The current study demonstrates that a stable CuO:Gra-COOH photocathode can also be synthesized using a solution technique. As a result, there is an open opportunity to expand solar H_2 generation on a large scale.

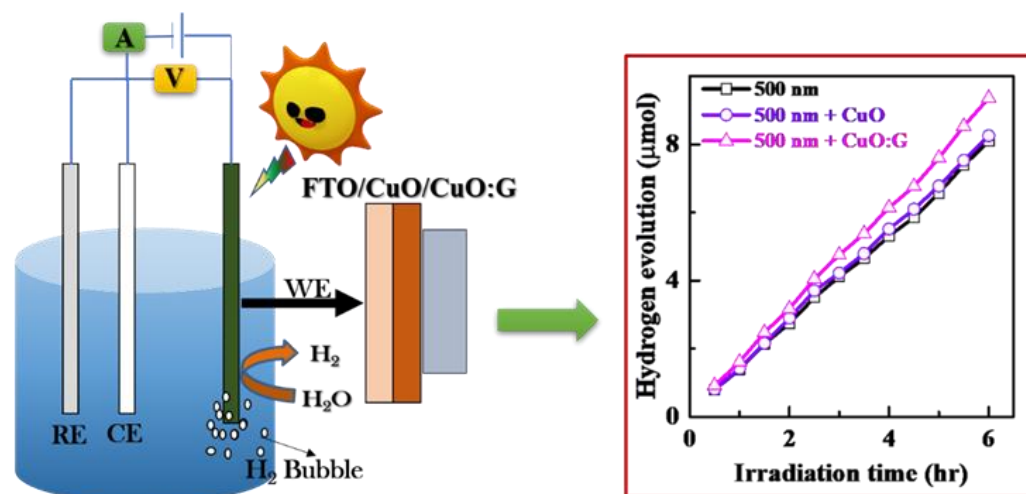


Figure 10. Hydrogen evolution under light illumination of a 500 nm sputter CuO and a 500 nm sputter CuO with sol-gel-deposited CuO and CuO:Gra-COOH charge-transfer layer.

3. Experimental Section

3.1. Thin-Film Preparation on FTO-Coated Glass Substrate

A CuO layer was sputtered at 500 nm thickness under identical circumstances as previously reported [67]. The thickness of sputter-grown CuO was ~ 500 nm, which is sufficient to absorb maximum visible light. Firstly, a 500 nm thick CuO film was grown on FTO (fluorine-doped tin oxide) substrate via sputtering, followed by sol-gel spin-coated thin film (~ 20 nm) of CuO and CuO:Gra-COOH that was deposited separately.

FTO-coated glass substrates were used to deposit CuO thin films. Before nitrogen gas dried, the substrates were ultrasonically cleaned in IPA for 10 min. The substrates were cleaned before being introduced into the CuO thin-film-sputtering chamber for deposition. CuO thin film with a thickness of 500 nm was deposited on FTO substrate by using sputter deposition. In an argon atmosphere, CuO target at 100 W was sputtered at a pressure of 3 mTorr. Rapid thermal annealing was performed after deposition to increase the crystal quality of the CuO film. Following that, samples were annealed in nitrogen at 600°C for 60 s (heating and cooling rate of $10^\circ\text{C}/\text{s}$) by rapid thermal treatment (RTT). CuO and incorporated graphene CuO thin film were then deposited on the sputter-grown CuO (500 nm)/FTO substrates via sol-gel/spin-coating technique, as shown in Figure 11a,b.

A copper oxide (CuO) solution was made by vigorously stirring 1.0 mL ethanolamine ($\text{C}_2\text{H}_7\text{NO}$) into 20 mL 2-methoxyethanol ($\text{C}_3\text{H}_8\text{O}_2$). After 15 min of constant stirring, 1.09 g copper (II) acetate ($\text{Cu}(\text{CH}_3\text{COO})_2$) was added to the above-mentioned solution, yielding a deep blue color. In addition, 0.5 mL polyethylene glycol ($\text{C}_{2n}\text{H}_{4n+2}\text{O}_{n+1}$) (average molecular weight 200) was added to the solution, and the solution was set to deposit as CuO film. Following that, 0.04 g-COOH functionalized graphene nanosheets (Cheap Tubes Inc., Cambridgeport, VT, USA) was added to 1 mL CuO solution, and then the solution was sonicated for 60 s by using pulse mode (5 s on and 5 s off). Before deposition on an FTO glass substrate, an additional 3 h of spin-coating stirring was performed, and the film was dried at 100°C on a hotplate for a couple of minutes just before annealing at 600°C for 10 min. The thickness of the sol-gel/spin-coat films deposited with CuO and CuO-Gra-COOH was approximately 20 nm.

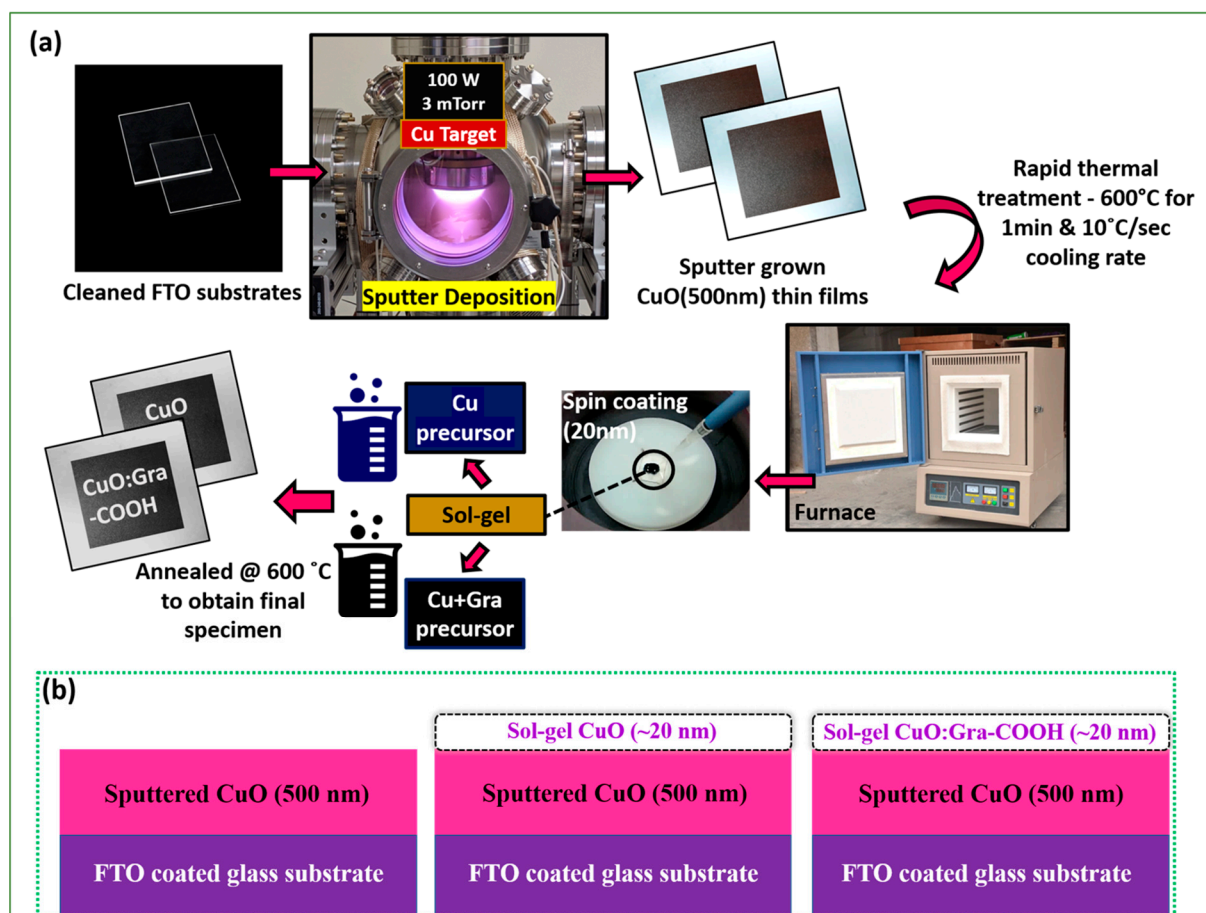


Figure 11. (a) Schematic diagram of sputter CuO-based photocathode fabrication with sol-gel spin-coated CuO and CuO:Gra-COOH charge-transfer layer. (b) Schematic diagram of sputter CuO-based photocathode with sol-gel spin-coated CuO and CuO:G-COOH charge-transfer layer. Schematic design of photoelectrodes.

3.2. Material Characterization

Diffraction and crystallographic information were recorded by X-ray diffractometer (Bruker D8 Advance, Billerica, MA, USA, Rigaku SmartLab, Tokyo, Japan and Panalytical X'Pert Pro, Almelo, The Netherlands) with Cu-K α radiation ($\lambda = 1.54 \text{ \AA}$). Morphological analysis was performed using high-resolution transmission electron microscopy (HRTEM) (JEOL JEM-2100F, FEI Tecnai F30, Portland, OR, USA) at resolutions ranging from 5 to 50 nm. Topographical and optical measurements were performed using atomic force microscopy (AFM) (Bruker Dimension Icon, Asylum Research MFP-3D, Billerica, MA, USA) and Agilent Cary 60 (Thermo Scientific Evolution 60S, Tokyo, Japan). The electronic structure and chemical state of the samples were evaluated by X-ray photoelectron spectroscopy (XPS) (Thermo Fisher Scientific K-Alpha, Waltham, MA, USA). UV-visible spectroscopy (Shimadzu UV-2600, Kyoto, Japan) was used to measure the catalytic properties of the samples.

3.3. Photoelectrochemical Measurement (PEC)

This study used a three-electrode cell configuration with a platinum foil as the counter electrode (C.E), Ag/AgCl as the reference electrode (R.E) and CuO thin films as the working electrode (W.E) to perform photoelectrochemical (PEC) experiments. The tests were performed in an electrolyte solution with a pH of 5.84 and a concentration of 0.1 M Na₂SO₄. Black tape was used to conceal the CuO thin film's 1 cm² active region. Using a Metrohm-Autolab PGSTAT101 potentiostat and a 150 W Xenon arc lamp with AM 1.5 filters, PEC characterization was carried out. The illuminating light on the CuO thin film was retained

at a constant 100 mWcm^{-2} intensity. The applied fixed potential and current density were 1.2 V and 0.5 mA cm^{-2} , respectively.

3.4. Computational Methodologies

All geometry optimizations were carried out using the B3LYP method in conjunction with 6–31G** and LANL2DZ basis sets. C, H, O and N atoms were treated with 6–31G**, and LANL2DZ was used for Cu. The optimized geometries were used to calculate energy levels, population analysis and molecular orbital analysis. All calculations were performed using Gaussian 16 code [68].

4. Conclusions

To summarize, we propose a simple, low-cost, scalable solution-based approach for fabricating and designing CuO:Gra-COOH photocathodes. We have shown that graphene incorporates nanoparticles into the CuO film, which improves the electrical and optical properties of the film. The -COOH functional group improves water-splitting performance with CuO electrode stability, and the PEC measurements confirm that H_2 evolution takes place. Gra:CuO-based films are used to obtain a picture of solar-driven WS for H_2 production and photocatalytic activity. The performance of PEC improves slightly with the addition of graphene nanoparticles due to increased film conductivity and the suppression of charge-carrier recombination. Additionally, it is observed that the graphene functional group plays a significant role in making more effective and stable photoelectrodes due to its electron-accepting tendency. According to the DFT calculations between different complexes of graphene with CuO, CuO@Gra-COOH shows the finest and most stable complex due to its high energy gap of 0.78 and charge distribution of $-0.81 |e|$. The presence of an ultra-thin CuO:Gra-COOH charge-transport layer shows $\sim 9.3 \mu\text{mol H}_2$ evolution. This work opens up the opportunity to improve the photocathode performance by integrating an ultra-thin charge-transport layer. Highly effective and stable photocathodes can be designed by combining a metal oxide/charge-transport layer for UV-visible light-driven solar H_2 production in practice, which is supported by extensive theoretical results.

Author Contributions: Conceptualization, G.K.D., S.B. and S.C.; methodology, A.M.S.K., B.R., P.B. and H.S.; writing—original draft, A.M.S.K., C.M., S.C. and G.K.D.; characterization, A.M.S.K., Y.-F.L., A.K. and B.R.; computational analysis, S.H., A.C., S.K., M.K.R. and B.C.; review and editing, S.R., S.C. and G.K.D.; supervision, G.K.D., S.R. and S.C.; project administration, G.K.D.; data curation, A.M.S.K., S.C. and G.K.D. All authors have read and agreed to the published version of the manuscript.

Funding: This work was funded by the NUS Resilience Growth Fund (Grant No. A-0000065-99-99).

Data Availability Statement: Data will be made available upon request to the corresponding author.

Acknowledgments: A.M.S.K. and S.C. would like to thank SRM University and AP Seed Research Funding for their financial support. Sajal Biring acknowledges financial support from the National Science and Technology Council, Taiwan, formerly known as the Ministry of Science and Technology, Taiwan, under grant no. MOST 111-2221-E-131-013.

Conflicts of Interest: The authors declare no conflict of interest.

References

1. Hernandez, R.R.; Armstrong, A.; Burney, J.; Ryan, G.; Moore-O’leary, K.; Diédhiou, I.; Grodsky, S.M.; Saul-Gershenz, L.; Davis, R.; Macknick, J.; et al. Techno-ecological synergies of solar energy for global sustainability. *Nat. Sustain.* **2019**, *2*, 560–568. [CrossRef]
2. Halabi, M.A.; Al-Qattan, A.; Al-Otaibi, A. Application of solar energy in the oil industry—Current status and future prospects. *Renew. Sustain. Energy Rev.* **2015**, *43*, 296–314. [CrossRef]
3. Rosen, M.A. Engineering Sustainability: A Technical Approach to Sustainability. *Sustainability* **2012**, *4*, 2270–2292. [CrossRef]
4. Sahoo, D.P.; Patnaik, S.; Rath, D.; Nanda, B.; Parida, K. Cu@CuO promoted g-C₃N₄/MCM-41: An efficient photocatalyst with tunable valence transition for visible light induced hydrogen generation. *RSC Adv.* **2016**, *6*, 112602–112613. [CrossRef]
5. Dangelico, R.M.; Pujari, D. Mainstreaming Green Product Innovation: Why and How Companies Integrate Environmental Sustainability. *J. Bus. Ethic* **2010**, *95*, 471–486. [CrossRef]

6. Dalapati, G.K.; Masudy-Panah, S.; Kumar, A.; Tan, C.C.; Tan, H.R.; Chi, D. Aluminium alloyed iron-silicide/silicon solar cells: A simple approach for low cost environmental-friendly photovoltaic technology. *Sci. Rep.* **2015**, *5*, 17810. [[CrossRef](#)]
7. Creissen, C.E.; Fontecave, M. Solar-Driven Electrochemical CO₂ Reduction with Heterogeneous Catalysts. *Adv. Energy Mater.* **2021**, *11*, 2002652. [[CrossRef](#)]
8. Tawfik, W.Z.; Hassan, M.A.; Johar, M.A.; Ryu, S.-W.; Lee, J.K. Highly conversion efficiency of solar water splitting over p-Cu₂O/ZnO photocatalyst grown on a metallic substrate. *J. Catal.* **2019**, *374*, 276–283. [[CrossRef](#)]
9. Walter, M.G.; Warren, E.L.; McKone, J.R.; Boettcher, S.W.; Mi, Q.; Santori, E.A.; Lewis, N.S. Solar Water Splitting Cells. *Chem. Rev.* **2010**, *110*, 6446–6473. [[CrossRef](#)]
10. Fujishima, A.; Honda, K. Electrochemical Photolysis of Water at a Semiconductor Electrode. *Nature* **1972**, *238*, 37–38. [[CrossRef](#)]
11. Grätzel, M. Photoelectrochemical Cells. In *Materials for Sustainable Energy*; Co-Published with Macmillan Publishers Ltd.: London, UK, 2010; pp. 26–32. [[CrossRef](#)]
12. Chen, H.M.; Chen, C.K.; Liu, R.-S.; Zhang, L.; Zhang, J.; Wilkinson, D.P. Nano-architecture and material designs for water splitting photoelectrodes. *Chem. Soc. Rev.* **2012**, *41*, 5654–5671. [[CrossRef](#)] [[PubMed](#)]
13. Dalapati, G.K.; Chua, C.S.; Kushwaha, A.; Liew, S.L.; Suresh, V.; Chi, D. All earth abundant materials for low cost solar-driven hydrogen production. *Mater. Lett.* **2016**, *183*, 183–186. [[CrossRef](#)]
14. Chen, Z.; Jaramillo, T.F.; Deutsch, T.G.; Kleiman-Shwarsstein, A.; Forman, A.J.; Gaillard, N.; Garland, R.; Takane, K.; Heske, C.; Sunkara, M.; et al. Accelerating materials development for photoelectrochemical hydrogen production: Standards for methods, definitions, and reporting protocols. *J. Mater. Res.* **2010**, *25*, 3–16. [[CrossRef](#)]
15. Masudy-Panah, S.; Dalapati, G.K.; Radhakrishnan, K.; Kumar, A.; Tan, H.R.; Kumar, E.N.; Vijila, C.; Tan, C.C.; Chi, D. p-CuO/n-Si heterojunction solar cells with high open circuit voltage and photocurrent through interfacial engineering. *Prog. Photovolt. Res. Appl.* **2015**, *23*, 637–645. [[CrossRef](#)]
16. Ahmed, A.M.; Abdalla, E.M.; Shaban, M. Simple and Low-Cost Synthesis of Ba-Doped CuO Thin Films for Highly Efficient Solar Generation of Hydrogen. *J. Phys. Chem. C* **2020**, *124*, 22347–22356. [[CrossRef](#)]
17. Sultana, J.; Paul, S.; Karmakar, A.; Dalapati, G.K.; Chattopadhyay, S. Optimizing the thermal annealing temperature: Technological route for tuning the photo-detecting property of p-CuO thin films grown by chemical bath deposition method. *J. Mater. Sci. Mater. Electron.* **2018**, *29*, 12878–12887. [[CrossRef](#)]
18. Dimopoulos, T.; Pei, A.; Müllner, P.; Neuschitzer, M.; Resel, R.; Abermann, S.; Postl, M.; List, E.J.W.; Yakunin, S.; Heiss, W.; et al. Photovoltaic properties of thin film heterojunctions with cupric oxide absorber. *J. Renew. Sustain. Energy* **2013**, *5*, 011205. [[CrossRef](#)]
19. Chiang, C.-Y.; Epstein, J.; Brown, A.; Munday, J.N.; Culver, J.N.; Ehrman, S. Biological Templates for Antireflective Current Collectors for Photoelectrochemical Cell Applications. *Nano Lett.* **2012**, *12*, 6005–6011. [[CrossRef](#)]
20. Yang, Y.; Xu, D.; Wu, Q.; Diao, P. Cu₂O/CuO Bilayered Composite as a High-Efficiency Photocathode for Photoelectrochemical Hydrogen Evolution Reaction. *Sci. Rep.* **2016**, *6*, 35158. [[CrossRef](#)]
21. Koffyberg, F.P.; Benko, F.A. A photoelectrochemical determination of the position of the conduction and valence band edges of p-type CuO. *J. Appl. Phys.* **1982**, *53*, 1173–1177. [[CrossRef](#)]
22. Wadia, C.; Alivisatos, A.P.; Kammen, D.M. Materials Availability Expands the Opportunity for Large-Scale Photovoltaics Deployment. *Environ. Sci. Technol.* **2009**, *43*, 2072–2077. [[CrossRef](#)] [[PubMed](#)]
23. Manojkumar, K.; Kandeegan, R.; Brindha, R.; Sangeetha, V.; Saminathan, K. Non-precious metal-based integrated electrodes for overall alkaline water splitting. *J. Indian Chem. Soc.* **2022**, *99*, 100775. [[CrossRef](#)]
24. Trang, T.; Tu, L.; Man, T.; Mathesh, M.; Nam, N.; Thu, V. A high-efficiency photoelectrochemistry of Cu₂O/TiO₂ nanotubes based composite for hydrogen evolution under sunlight. *Compos. Part B Eng.* **2019**, *174*, 106969. [[CrossRef](#)]
25. Quyen, V.T.; Jitae, K.; Huong, P.T.; Ha, L.T.T.; Thanh, D.M.; Viet, N.M.; Thang, P.Q. Copper doped titanium dioxide as a low-cost visible light photocatalyst for water splitting. *Sol. Energy* **2021**, *218*, 150–156. [[CrossRef](#)]
26. Negi, C.; Kandwal, P.; Rawat, J.; Sharma, M.; Sharma, H.; Dalapati, G.; Dwivedi, C. Carbon-doped titanium dioxide nanoparticles for visible light driven photocatalytic activity. *Appl. Surf. Sci.* **2021**, *554*, 149553. [[CrossRef](#)]
27. Chatterjee, P.; Ambati, M.S.K.; Chakraborty, A.K.; Chakraborty, S.; Biring, S.; Ramakrishna, S.; Wong, T.K.S.; Kumar, A.; Lawaniya, R.; Dalapati, G.K. Photovoltaic/photo-electrocatalysis integration for green hydrogen: A review. *Energy Convers. Manag.* **2022**, *261*, 115648. [[CrossRef](#)]
28. Bamola, P.; Sharma, M.; Dwivedi, C.; Singh, B.; Ramakrishna, S.; Dalapati, G.K.; Sharma, H. Interfacial interaction of plasmonic nanoparticles (Ag, Au) decorated floweret TiO₂ nanorod hybrids for enhanced visible light driven photocatalytic activity. *Mater. Sci. Eng. B* **2021**, *273*, 115403. [[CrossRef](#)]
29. Dey, A.; Chandrabose, G.; Dampney, L.A.; Erakulan, E.; Thapa, R.; Zhuk, S.; Dalapati, G.K.; Ramakrishna, S.; Braithwaite, N.S.J.; Shirzadi, A.; et al. Cu₂O/CuO heterojunction catalysts through atmospheric pressure plasma induced defect passivation. *Appl. Surf. Sci.* **2021**, *541*, 148571. [[CrossRef](#)]
30. Pinaud, B.A.; Benck, J.D.; Seitz, L.C.; Forman, A.J.; Chen, Z.; Deutsch, T.G.; James, B.D.; Baum, K.N.; Baum, G.N.; Ardo, S.; et al. Technical and economic feasibility of centralized facilities for solar hydrogen production via photocatalysis and photoelectrochemistry. *Energy Environ. Sci.* **2013**, *6*, 1983–2002. [[CrossRef](#)]
31. Dalapati, G.K.; Masudy-Panah, S.; Moakhar, R.S.; Chakraborty, S.; Ghosh, S.; Kushwaha, A.; Katal, R.; Chua, C.S.; Xiao, G.; Tripathy, S.; et al. Nanoengineered Advanced Materials for Enabling Hydrogen Economy: Functionalized Graphene-Incorporated Cupric Oxide Catalyst for Efficient Solar Hydrogen Production. *Glob. Chall.* **2020**, *4*, 1900087. [[CrossRef](#)]

32. Lim, Y.-F.; Chua, C.S.; Lee, C.J.J.; Chi, D. sol-gel deposited Cu₂O and CuO thin films for photocatalytic water splitting. *Phys. Chem. Chem. Phys.* **2014**, *16*, 25928–25934. [[CrossRef](#)] [[PubMed](#)]
33. Masudy-Panah, S.; Radhakrishnan, K.; Kumar, A.; Wong, T.I.; Yi, R.; Dalapati, G.K. Optical bandgap widening and phase transformation of nitrogen doped cupric oxide. *J. Appl. Phys.* **2015**, *118*, 225301. [[CrossRef](#)]
34. Masudy-Panah, S.; Radhakrishnan, K.; Tan, H.R.; Yi, R.; Wong, T.I.; Dalapati, G.K. Titanium doped cupric oxide for photovoltaic application. *Sol. Energy Mater. Sol. Cells* **2015**, *140*, 266–274. [[CrossRef](#)]
35. Hasan, R.; Hamid, S.B.A.; Basirun, W.J.; Suhaimy, S.H.M.; Mat, A.N.C. A sol-gel derived, copper-doped, titanium dioxide-reduced graphene oxide nanocomposite electrode for the photoelectrocatalytic reduction of CO₂ to methanol and formic acid. *RSC Adv.* **2015**, *5*, 77803–77813. [[CrossRef](#)]
36. Chen, D.; Zhang, H.; Liu, Y.; Li, J. Graphene and its derivatives for the development of solar cells, photoelectrochemical, and photocatalytic applications. *Energy Environ. Sci.* **2013**, *6*, 1362–1387. [[CrossRef](#)]
37. Fan, W.; Yu, X.; Lu, H.-C.; Bai, H.; Zhang, C.; Shi, W. Fabrication of TiO₂/RGO/Cu₂O heterostructure for photoelectrochemical hydrogen production. *Appl. Catal. B Environ.* **2016**, *181*, 7–15. [[CrossRef](#)]
38. Mateo, D.; Esteve-Adell, I.; Albero, J.; Primo, A.; García, H. Oriented 2.0.0 Cu₂O nanoplatelets supported on few-layers graphene as efficient visible light photocatalyst for overall water splitting. *Appl. Catal. B Environ.* **2017**, *201*, 582–590. [[CrossRef](#)]
39. Loh, K.P.; Bao, Q.; Eda, G.; Chhowalla, M. Graphene oxide as a chemically tunable platform for optical applications. *Nat. Chem.* **2010**, *2*, 1015–1024. [[CrossRef](#)]
40. Chen, D.; Feng, H.; Li, J. Graphene Oxide: Preparation, Functionalization, and Electrochemical Applications. *Chem. Rev.* **2012**, *112*, 6027–6053. [[CrossRef](#)]
41. Beitollahi, H.; Garkani-Nejad, F.; Tajik, S.; Ganjali, M.R. Voltammetric determination of acetaminophen and tryptophan using a graphite screen printed electrode modified with functionalized graphene oxide nanosheets within a Fe₃O₄@SiO₂ nanocomposite. *Iran. J. Pharm. Res.* **2019**, *18*, 80–90. [[CrossRef](#)]
42. El-Hout, S.; El-Sheikh, S.; Hassan, H.M.; Harraz, F.A.; Ibrahim, I.; El-Sharkawy, E. A green chemical route for synthesis of graphene supported palladium nanoparticles: A highly active and recyclable catalyst for reduction of nitrobenzene. *Appl. Catal. A Gen.* **2015**, *503*, 176–185. [[CrossRef](#)]
43. Cheng, Y.; Fan, Y.; Pei, Y.; Qiao, M. Graphene-supported metal/metal oxide nanohybrids: Synthesis and applications in heterogeneous catalysis. *Catal. Sci. Technol.* **2015**, *5*, 3903–3916. [[CrossRef](#)]
44. Ma, B.; Wang, Y.; Tong, X.; Guo, X.; Zheng, Z.; Guo, X. Graphene-supported CoS₂ particles: An efficient photocatalyst for selective hydrogenation of nitroaromatics in visible light. *Catal. Sci. Technol.* **2017**, *7*, 2805–2812. [[CrossRef](#)]
45. Xie, G.; Zhang, K.; Guo, B.; Liu, Q.; Fang, L.; Gong, J.R. Graphene-Based Materials for Hydrogen Generation from Light-Driven Water Splitting. *Adv. Mater.* **2013**, *25*, 3820–3839. [[CrossRef](#)] [[PubMed](#)]
46. Geim, A.K. Graphene: Status and Prospects. *Science* **2009**, *324*, 1530–1534. [[CrossRef](#)]
47. Ragupathy, M.; Ramasubramanian, B.; Rajagopalan, K.; Ganesan, A. Electrocatalytic response of the modified ZnO-G electrodes towards the oxidation of serotonin with multi metallic corrosion protection. *J. Indian Chem. Soc.* **2022**, *99*, 100768. [[CrossRef](#)]
48. Kou, R.; Shao, Y.; Mei, D.; Nie, Z.; Wang, D.; Wang, C.; Viswanathan, V.V.; Park, S.; Aksay, I.A.; Lin, Y.; et al. Stabilization of Electrocatalytic Metal Nanoparticles at Metal–Metal Oxide–Graphene Triple Junction Points. *J. Am. Chem. Soc.* **2011**, *133*, 2541–2547. [[CrossRef](#)]
49. Liu, M.; Zhang, R.; Chen, W. Graphene-Supported Nanoelectrocatalysts for Fuel Cells: Synthesis, Properties, and Applications. *Chem. Rev.* **2014**, *114*, 5117–5160. [[CrossRef](#)]
50. Arshad, A.; Iqbal, J.; Siddiq, M.; Ali, M.U.; Ali, A.; Shabbir, H.; Bin Nazeer, U.; Saleem, M.S. Solar light triggered catalytic performance of graphene-CuO nanocomposite for waste water treatment. *Ceram. Int.* **2017**, *43*, 10654–10660. [[CrossRef](#)]
51. Burke, K. Perspective on density functional theory. *J. Chem. Phys.* **2012**, *136*, 150901. [[CrossRef](#)] [[PubMed](#)]
52. Geerlings, P.; De Proft, A.F.; Langenaeker, W. Conceptual Density Functional Theory. *Chem. Rev.* **2003**, *103*, 1793–1874. [[CrossRef](#)]
53. Harvey, J.N. On the accuracy of density functional theory in transition metal chemistry. *Annu. Rep. Sect. C Phys. Chem.* **2006**, *102*, 203–226. [[CrossRef](#)]
54. Minenkov, Y.; Singstad, Å.; Occhipinti, G.; Jensen, V.R. The accuracy of DFT-optimized geometries of functional transition metal compounds: A validation study of catalysts for olefin metathesis and other reactions in the homogeneous phase. *Dalton Trans.* **2012**, *41*, 5526–5541. [[CrossRef](#)] [[PubMed](#)]
55. Raji, M.; Essabir, H.; Rodrigue, D.; Bouhfid, R.; Qaiss, A.E.K. Influence of graphene oxide and graphene nanosheet on the properties of polyvinylidene fluoride nanocomposites. *Polym. Compos.* **2017**, *39*, 2932–2941. [[CrossRef](#)]
56. Ain, Q.T.; Haq, S.H.; Alshammari, A.; Al-Mutlaq, M.A.; Anjum, M.N. The systemic effect of PEG-nGO-induced oxidative stress in vivo in a rodent model. *Beilstein J. Nanotechnol.* **2019**, *10*, 901–911. [[CrossRef](#)]
57. Wang, Z.; Xiao, Y.; Cui, X.; Cheng, P.; Wang, B.; Gao, Y.; Li, X.; Yang, T.; Zhang, T.; Lu, G. Humidity-Sensing Properties of Urchinlike CuO Nanostructures Modified by Reduced Graphene Oxide. *ACS Appl. Mater. Interfaces* **2014**, *6*, 3888–3895. [[CrossRef](#)] [[PubMed](#)]
58. Arivazhagan, M.; Manivel, S.; Jeyavijayan, S.; Meenakshi, R. Vibrational spectroscopic (FTIR and FT-Raman), first-order hyperpolarizability, HOMO, LUMO, NBO, Mulliken charge analyses of 2-ethylimidazole based on Hartree–Fock and DFT calculations. *Spectrochim. Acta Part A Mol. Biomol. Spectrosc.* **2015**, *134*, 493–501. [[CrossRef](#)]
59. Bell, N.J.; Ng, Y.H.; Du, A.; Coster, H.; Smith, S.C.; Amal, R. Understanding the Enhancement in Photoelectrochemical Properties of Photocatalytically Prepared TiO₂-Reduced Graphene Oxide Composite. *J. Phys. Chem. C* **2011**, *115*, 6004–6009. [[CrossRef](#)]

60. Tian, G.; Li, H.; Ma, W.; Wang, Y. Substituent effects in π -stacking of histidine on functionalized-SWNT and graphene. *Comput. Theor. Chem.* **2015**, *1062*, 44–49. [[CrossRef](#)]
61. Ionita, M.; Crica, L.E.; Vasile, E.; Dinescu, S.; Pandele, M.A.; Costache, M.; Haugen, H.J.; Iovu, H. Effect of carboxylic acid functionalized graphene on physical-chemical and biological performances of polysulfone porous films. *Polymer* **2016**, *92*, 1–12. [[CrossRef](#)]
62. Cheng, L.; Wang, Y.; Huang, D.; Nguyen, T.; Jiang, Y.; Yu, H.; Ding, N.; Ding, G.; Jiao, Z. Facile synthesis of size-tunable CuO/graphene composites and their high photocatalytic performance. *Mater. Res. Bull.* **2015**, *61*, 409–414. [[CrossRef](#)]
63. Fampiou, I.; Ramasubramaniam, A. Binding of Pt Nanoclusters to Point Defects in Graphene: Adsorption, Morphology, and Electronic Structure. *J. Phys. Chem. C* **2012**, *116*, 6543–6555. [[CrossRef](#)]
64. Zhen, Y.; Reddy, V.S.; Ramasubramanian, B.; Ramakrishna, S. Three-Dimensional AgNps@Mxene@PEDOT:PSS Composite Hybrid Foam as a Piezoresistive Pressure Sensor with Ultra-Broad Working Range. *J. Mater. Sci.* **2022**, *57*, 21960–21979. [[CrossRef](#)] [[PubMed](#)]
65. Yu, Y.-H.; Chen, Y.-P.; Cheng, Z. Microwave-assisted synthesis of rod-like CuO/TiO₂ for high-efficiency photocatalytic hydrogen evolution. *Int. J. Hydrogen Energy* **2015**, *40*, 15994–16000. [[CrossRef](#)]
66. Zhang, T.; Liu, H.; Han, X.; Biset-Peiró, M.; Yang, Y.; Imaz, I.; Maspoch, D.; Yang, B.; Morante, J.R.; Arbiol, J. Improvement of carbon dioxide electroreduction by crystal surface modification of ZIF-8. *Dalton Trans.* **2023**, *11*, 5460–5475. [[CrossRef](#)] [[PubMed](#)]
67. Masudy-Panah, S.; Moakhar, R.S.; Chua, C.S.; Tan, H.R.; Wong, T.I.; Chi, D.; Dalapati, G.K. Nanocrystal Engineering of Sputter-Grown CuO Photocathode for Visible-Light-Driven Electrochemical Water Splitting. *ACS Appl. Mater. Interfaces* **2016**, *8*, 1206–1213. [[CrossRef](#)]
68. Frisch, M.J.; Trucks, G.W.; Schlegel, H.B.; Scuseria, G.E.; Robb, M.A.; Cheeseman, J.R.; Scalmani, G.; Barone, V.; Petersson, G.A.; Nakatsuji, H.; et al. *Gaussian 16, Revision C.01*; Gaussian, Inc.: Wallingford, CT, USA, 2016.

Disclaimer/Publisher’s Note: The statements, opinions and data contained in all publications are solely those of the individual author(s) and contributor(s) and not of MDPI and/or the editor(s). MDPI and/or the editor(s) disclaim responsibility for any injury to people or property resulting from any ideas, methods, instructions or products referred to in the content.